Received: 10 March 2021 | Revised: 29 May 2021 | Accepted: 16 June 2021

DOI: 10.4218/etrij.2021-0053

SPECIAL ISSUE

ETRI Journal WILEY

Automatic wall slant angle map generation using 3D point clouds

Jeongyun Kim[1] | **Seungsang Yun**[2] | **Minwoo Jung**[1] | **Ayoung Kim**[1] | **Younggun Cho**[3]

[1]Department of Civil and Environmental Engineering, KAIST, Daejeon, Rep. of Korea

[2]Robotics Program, KAIST, Daejeon, Rep. of Korea

[3]Department of Robotics Engineering, Yeungnam University, Gyeongsan, Rep. of Korea

Correspondence
Younggun Cho, Department of Robotics Engineering, Yeungnam University, Gyeongsan, Rep. of Korea.
Email: yg.cho@yu.ac.kr

Funding information
Urban Declining Area Regenerative Capacity-Enhancing Technology Research Program funded by Ministry of Land, Infrastructure, and Transport of Korean government, Grant/Award Number: 21TSRD-B151228-03

Recently, quantitative and repetitive inspections of the old urban area were conducted because many structures exceed their designed lifetime. The health of a building can be validated from the condition of the outer wall, while the slant angle of the wall widely serves as an indicator of urban regeneration projects. Mostly, the inspector directly measures the inclination of the wall or partially uses 3D point measurements using a static light detection and ranging (LiDAR). These approaches are costly, time-consuming, and only limited space can be measured. Therefore, we propose a mobile mapping system and automatic slant map generation algorithm, configured to capture urban environments online. Additionally, we use the LiDAR-inertial mapping algorithm to construct raw point clouds with gravity information. The proposed method extracts walls from raw point clouds and measures the slant angle of walls accurately. The generated slant angle map is evaluated in indoor and outdoor environments, and the accuracy is compared with real tiltmeter measurements.

KEYWORDS
Inertial measurement unit, LiDAR, Mapping, simultaneous localization and mapping, structural health monitoring

1 | INTRODUCTION

Nowadays, structural health monitoring is a major essential process that quantitatively inspects structural degradation. Its typical target is a single structure, such as a bridge, dam, or building. However, when there is a need to examine a group of buildings, such as several buildings in town, automation becomes a critical factor. Inspecting a group of buildings in blocks necessitates large-scale mapping accompanied by an automatic structural element extraction. Many risk factors in an underdeveloped city require redevelopment. Among them, the slant angle of the old building wall is an essential factor directly related to the occupants' safety and an important factor in judging the priority of redevelopment.

To measure a slanted wall for safety, researchers devised a method that automatically measures the slant angle of the wall using a camera and light detection and ranging (LiDAR). Cameras and LiDARs have been widely adopted in these studies. Tareen and Khan [1] developed mobile robots with a stereo camera rig for slope detection and calculation. Unfortunately, this method has limitations when the walls are not flat surfaces. Lv et al. [2] investigated the slope and edge detection indoor using two-dimensional (2D) extended Kalman filter simultaneous localization and mapping (SLAM). Their approach was unable to achieve three-dimensional (3D) solutions due to the large memory and high computational costs. Meng et al. [3] proposed a method for slant angle detection using 3D LiDAR targeting quadruped robots. These legged robot platform fits better for the uneven terrain; however, their solution showed limitations in handling many dynamic objects of cars and people in real time. Mao et al. [4] used small aircraft systems for damage assessment structures. This method is efficient for observing damaged structures, such as bridges or roads. Because our target environments are densely populated residential areas, we select a backpack-style mapping system to scan walls in narrows streets. Also, our method leverages inertial measurements for slant angle detection and refinement.

To overcome the above limitations, our method constructs a wall slant angle map using the LiDAR-inertial SLAM framework. In the proposed method, LiDAR and inertial measurement unit (IMU) are comprehensively used to capture information in point clouds. The proposed framework enables automatic and quantitative risk analysis of residents in an underdeveloped area. The main contributions of this paper are as follows:

- We present a systematic solution for slant angle map generation using LiDAR-inertial SLAM and construct a gravity-incorporated map for automatically computing the slant angle. Leveraging LiDAR with IMU allowed the robust map generation to the ego-motion when applied to the backpack-style mapping platform.
- We extract walls automatically using sliding window voting and clustering. By piping into random sample consensus (RANSAC) followed by a singular value decomposition (SVD), the outlier-removed-wall point cloud can be leveraged to complete the wall extraction. Here, we examine the eigenvalue ratio of the projected inlier points and classify nonwall objects and structures (for example, bushes and trees) to generate a more accurate wall map.
- We validate the proposed method using real walls with various curvatures. The overall framework runs automatically without requiring manual intervention over the 140 m by 95 m area coverage.

2 | RELATED WORKS

2.1 | Simultaneous localization and mapping

Early works in the LiDAR SLAM stems from a point cloud registration using Generalized Iterated Closest Point (GICP) [5] and Iterated Closest Point (ICP) [6]. This pairwise registration was further developed to compute the transformation between two consecutive frames: namely *LiDAR odometry*. During the registration process, point-to-point distance or point-to-plane distance was used for pose estimation. Seminar LiDAR SLAM studies include LiDAR odometry and mapping (LOAM) [7] and lightweight and ground-optimized lightweight and ground-optimized LiDAR odometry and mapping (LeGO-LOAM) [8].

Unlike these studies that only relied on LiDAR sensors, the combination of IMU and global positioning system (GPS) have been investigated. LiDAR inertial odometry via smoothing and mapping (LIO-SAM) proposed in Shan et al. [9] combines LiDAR SLAM with IMU preintegration factor [10] to complete the egocentric LiDAR-inertial state estimator. By tightly coupling LiDAR and IMU, the accuracy of point clouds was improved. For example, robocentric LiDAR-inertial state estimator for robust and efficient navigation (R-LINS) [11] used other sensors, except the IMU with small continuous drift accumulation when running a long time and results in inaccuracy. Recently, LIO-SAM used IMU measurements for sequential motion estimation and equally used the LiDAR pose from the IMU graph for the initial pose of LiDAR-based pose graph. The algorithm updated the IMU graph by incorporating the LiDAR pose. These procedures secure the reliability of localization and mapping results under fast motion and accuracy of point clouds. Also, GPS signals between several keyframes served as pose graph factors and produced a more accurate results. In this paper, we adopt LIO-SAM for creating the initial point cloud map from which we construct a slant angle map.

2.2 | Slant angle measurement

Measuring the slant angle of walls by scanning surrounding topographic features is essential for monitoring structural health or autonomous driving. Various studies have been dedicated to measuring slant angles. In Tareen and Khan [1], two ultrasonic sensors were used for autonomous driving and can measure the slant angle using the distance obtained by both sensors and the angle between the robot and ultrasonic sensors. However, the accuracy of this measurement depends on wind or temperature, and interference may occur between each sensor.

Lv et al. [2] used two 2D LiDARs instead of ultrasonic sensors for autonomous driving. The line segment feature was extracted from the surrounding environment using a vertical and horizontal LiDAR. Then, the slant angle was measured by comparing and using the two features. While it provided improved measurement accuracy than ultrasonic sensors, their maps were limited because a 2D map failed to recognize the discontinuous slant angle in the same wall. A large error occurs when the 3D structural variation exists (for example, uneven ground).

To overcome these limitations in 3D, Meng et al. [3] used 3D LiDAR to scan the surrounding environment and obtained a point cloud. Their approach removed the noise from the point cloud using a bilateral filter after which plane fitting progresses using RANSAC [12]. During this process, the slant angle was estimated. However, their study was limited to slant angle detection without performing map construction. Moreover, extracting discontinuous slant angle values remains a challenging issue. Thus, the point cloud and map construction are essential to accommodate various slant angles accordingly.

3 | METHOD

3.1 | Mapping system

We developed the mapping platform in a backpack format to scan uneven terrain with a narrow aisle. Figure 1 shows the system configuration used for the data acquisition with a detailed sensor specification presented in Table 1.

In the system, the 3D LiDAR develops a 3D point cloud map for wall extraction. The slant angle measurement is critically affected by gravity because the slant angle indicates the angle between the normal vectors of the wall and gravity. The IMU serves for the map generation under motion and gravity direction measures.

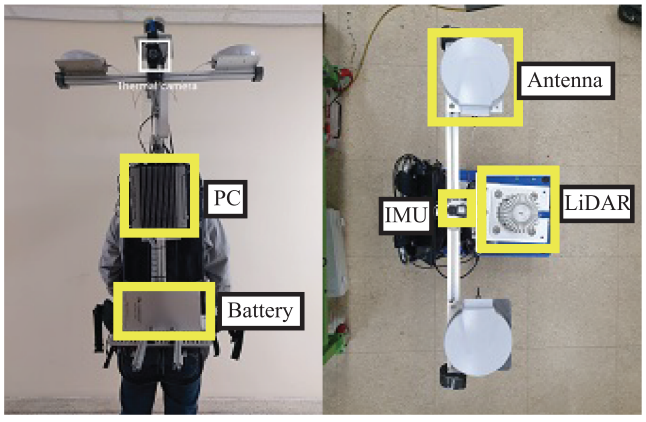

FIGURE 1 Light detection and ranging (LiDAR)-inertial measurement unit (IMU) backpack system

TABLE 1 Sensor list and specification

Type	Model	Description
LiDAR	Ouster (OS1-64)	64 channel 360° FOV, Range 120 m 10 Hz to 20 Hz
IMU	Microstrain (3dm-gx5-25 AHRS)	1000 Hz

3.2 | Overview

First, we create the initial 3D map using LiDAR-inertial SLAM, called LIO-SAM. From the initial map, we perform a coarse wall extraction using a windowed voting algorithm. These coarse walls are clustered using -density-based spatial clustering of applications with noise (DBSCAN) and *K*-means clustering. The resulting clustered and refined walls are piped into the model fitting module to compute the normal vectors by plane fitting using RANSAC and SVD. Finally, we find the angle between gravity and further refinements more accurately correct the roughly obtained wall points. The overall process is depicted in Figure 2. Also, the algorithm is described in Algorithm 1. In the following sections, each module is explained in detail.

Algorithm 1 Wall slant angle estimation

Input: $\mathcal{M}, \boldsymbol{g} \leftarrow$ LIO-SAM
$\mathcal{P}_{proj} \leftarrow \textsc{Projection}(\mathcal{M})$
$\hat{\mathcal{P}}_w \leftarrow \textsc{Classification}(\mathcal{W}_{i,j}, \epsilon)$
$k \leftarrow \text{DBSCAN}(\hat{\mathcal{P}}_w)$
for $l = 1 : k$ **do**
  $\mathcal{P}_R \leftarrow \text{RANSAC}(\mathcal{P}_k)$
  $\gamma \leftarrow \text{EIG}\,(\text{Cov}(\mathcal{P}_R))$ ▷ Equation (5)
  if $\gamma > 1.7$ **then**
    $\boldsymbol{n} \leftarrow \text{SVD}(\mathcal{P}_R)$
    $\theta_k = \arccos \frac{\boldsymbol{g}^\top \boldsymbol{n}}{|\boldsymbol{g}||\boldsymbol{n}|}$
  end if
end for
Output: θ_k

3.3 | LiDAR-inertial SLAM

To generate initial map points, we employ the LiDAR-inertial SLAM (LIO-SAM). Unlike existing methods that

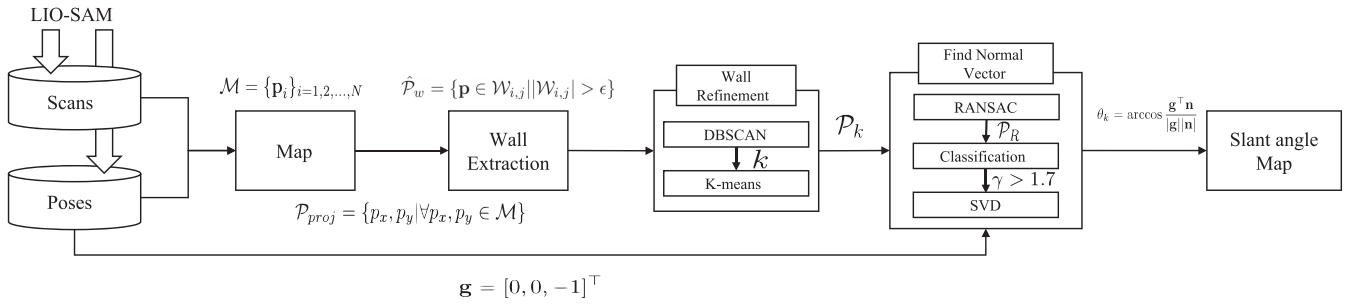

FIGURE 2 Diagram of the proposed method. The proposed method consists of four modules: light detection and ranging (LiDAR)-inertial simultaneous localization and mapping (SLAM), wall extraction, wall refinement, and slant angle analysis

focused on a single structure or a building, our interest is in covering a complex of buildings on a larger scale. To achieve this, coverage and scalability of the initial map generation are both critical factors.

LIO-SAM is the current state-of-the-art method in LiDAR-inertial SLAM. Introducing the preintegration factor in the graph SLAM framework yields mapping performance robust to the motion perturbation of LIO-SAM. The computed map is compensated with gravity because the IMU measures the direction of gravity.

By using LIO-SAM, we obtain the gravity considered initial map point cloud ($\mathcal{M}$) including Nnumber of points $\mathbf{p} = [p_x, p_y, p_z]^\top$:

$$\mathcal{M} = \{\mathbf{p}_i\}_{i=1,2,\ldots,N}, \tag{1}$$

with the gravity direction as minus the z direction (that is, $\mathbf{g} = [0, 0, -1]^\top$). Here, N is the number of elements in the set $\mathcal{M}$ ($N = |\mathcal{M}|$). This simplifies the complex computation; we will compute the angle between the normal vector and gravity.

3.4 | Wall extraction

Wall extraction using window voting is performed from the initial point cloud map $\mathcal{M}$. The points on the wall structures have similar x and y positions against varying z values (height). We project the initial 3D map onto the xy-plane ($\mathcal{P}_{\text{proj}}$) and count the number of points falling into a sliding window of size 1 m × 1 m ($\mathcal{W}_{i,j}$) as shown in Figure 3. If the number of points in this window is larger than the threshold ($\epsilon = 500$), the points become wall candidates.

$$\mathcal{P}_{\text{proj}} = \{p_x, p_y | \forall p_x, p_y \in \mathcal{M}\}, \tag{2}$$

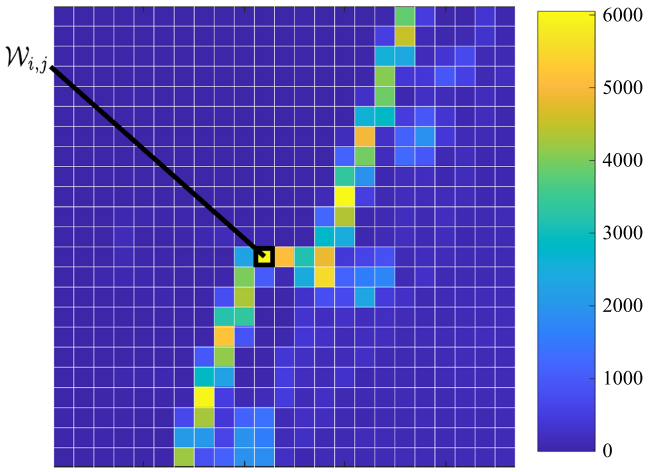

FIGURE 3 Sample view for window voting. In this top-down view of the 23 m by 23 m area, each grid represents a window with a size of 1 m by 1 m. For example, $\mathcal{W}_{i,j}$ is a set of points in the (i,j) window. Each cell (window) has color codes, which represents the number of points in the cell (window) $\mathcal{W}_{i,j}$

$$\mathcal{P}_{\text{proj}} = \bigcup_{i,j} \mathcal{W}_{i,j}, \tag{3}$$

$$\hat{\mathcal{P}}_w = \{\mathbf{p} \mid \mathbf{p} \in \mathcal{W}_{i,j}, |\mathcal{W}_{i,j}| > \epsilon\}. \tag{4}$$

3.5 | Wall refinement using clusters

We further refine the obtained rough wall points $\hat{\mathcal{P}}_w$ to extract a more accurate walls. We introduce two-step clustering methods to segment walls from the initial wall points. Specifically, we combine DBSCAN and K-means clustering to cluster points without knowing the number of clusters in advance. First, we apply DBSCAN to the initially segregated wall points [13]. Because DBSCAN is a connection-based clustering method, the cluster numbers are not needed. Figure 4A shows a sample cluster. This DBSCAN-clustered point $\mathcal{P}_D$ is examined to

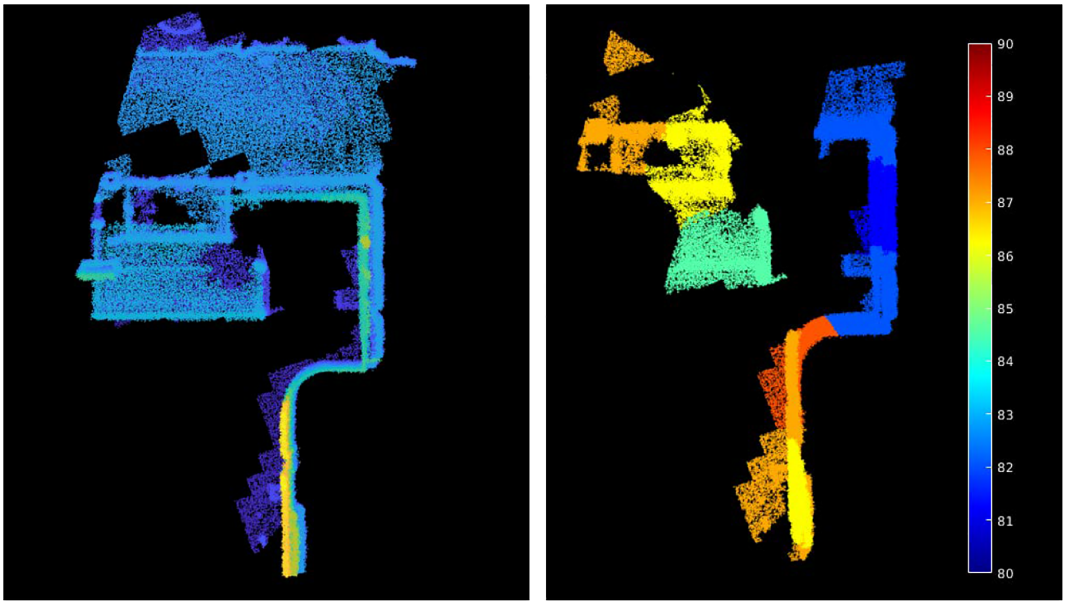

FIGURE 4 (A) Point cloud clustered using density-based spatial clustering of applications with noise (DBSCAN). (B) Using rough clusters computed from DBSCAN, the points are further refined using the *K*-means clustering. In (B), color means clustered walls. (A) shows that DBSCAN recognizes that it is a single wall and (B) is divided into 10 walls

determine the number of clusters k used in K-means clustering as follows:

$$k = \left\lceil \left| \frac{\mathcal{P}_D}{400} \right| \right\rceil. \tag{5}$$

At the end of this clustering module, we obtain K-mean clustered points $\mathcal{P}_K$ for the model fitting. Figure 4B shows the resulting K-mean clustered points.

3.6 | Slant angle analysis

3.6.1 | Outlier rejection using RANSAC

Model fitting is the last phase in computing the wall slant angle. By combining RANSAC and SVD, we exclude outliers and find the optimal plane parameters. The clustered point can contain outliers. Although the clean range measurement is achieved, the curved surface can include points deteriorating the plane fitting. Thus, we apply RANSAC before optimizing with SVD to ameliorate this issue. Given the clustered point cloud $\mathcal{P}_k$, we use the plane model $\hat{\mathbf{n}}^\top \mathbf{p} + d = 0$ to sort inliers and obtain initial plane normal estimation $\hat{\mathbf{n}} = [\hat{n}_x, \hat{n}_y, \hat{n}_z]^\top$.

3.6.2 | Nonwall object elimination and slant angle estimation

Even after the RANSAC-based rejection, nonwall objects close to the structure remain and alter the calculation of the slant angle. We exploit the singular value of the point cloud matrix to classify nonwall objects: trees and bushes. By examining the eigenvalue ratio of the point cloud distribution from the projected view, we determine if the points belong to a wall. According to Lalonde et al. [14], the eigenvalues of the covariance can be used to classify the objects. Differing from Lalonde et al. [14], we focus on the projected point cloud distribution because our aim is a binary classification. Specifically, walls have a large ratio between two singular values, while bushes and trees reveal a relatively small singular value ratio ($\gamma > 1.7$ was considered as nonwall objects in this study).

$$\gamma = \frac{\lambda_1}{\lambda_2}, \text{ where } \lambda_1 > \lambda_2. \tag{6}$$

From the points classified as wall, the inlier point cloud after RANSAC $\mathcal{P}_R$ is then piped into SVD to optimize the normal vector $\mathbf{n}$. Then, using this normal vector estimation and the gravity direction computed from LIO-SAM, we compute the slant angle of the wall as follows:

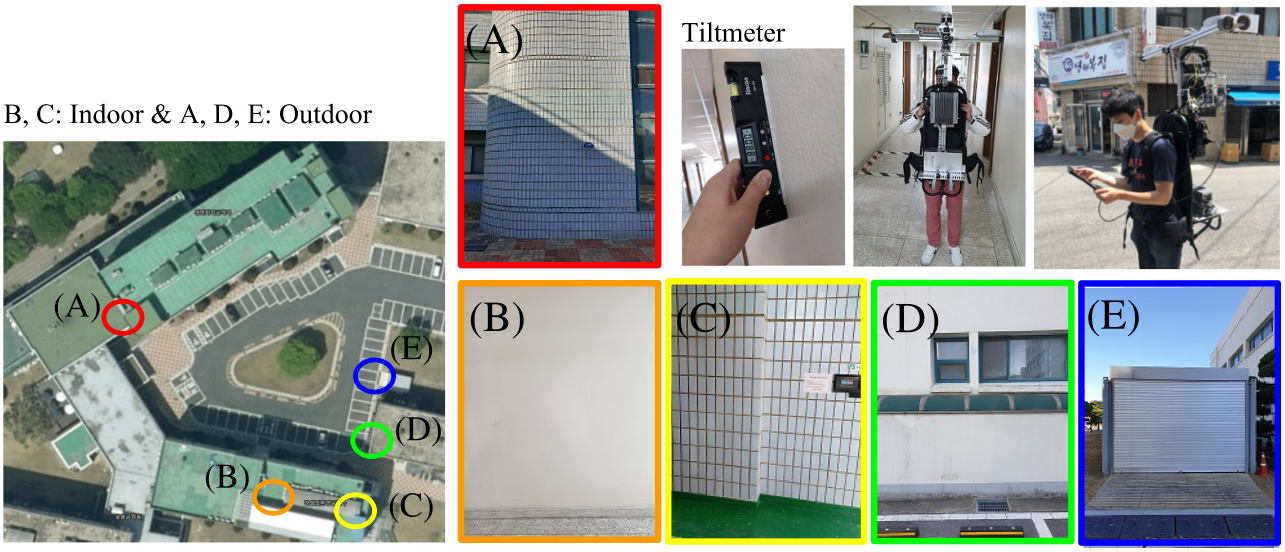

FIGURE 5 Experimental setup and test environments. We performed the tests indoors and outdoors while wearing the backpack system. Five walls are selected for evaluation (A to E). Using a tiltmeter, we obtain the baseline for the wall slant angle

TABLE 2 Five wall samples and their characteristics

Sample	Color	Indoor/Outdoor	Description
A	Red box	Outdoor	The wall is curved on the left edge.
B	Orange box	Indoor	The wall has constant slant angle.
C	Yellow box	Indoor	The wall consists of two walls having the same slant angle.
D	Green box	Outdoor	In the wall, the curved and the flat surface coexist. The materials of these two surfaces are different.
E	Blue	Outdoor	The surface is the sliding door with a constant slant angle.

$$\theta_k = \arccos\frac{\mathbf{g}^\top \mathbf{n}}{|\mathbf{g}||\mathbf{n}|}. \tag{7}$$

$$E_{deg} = \sqrt{\frac{\sum_{i=1}^{M}(\theta_i - \bar{\theta}_i)^2}{M}}. \tag{8}$$

4 | EXPERIMENTS

4.1 | Experiment setup

To evaluate the proposed method, we conducted a set of experiments in indoor and outdoor environments. The backpack system is worn and carried across the environment, as shown in Figure 5.

The details of the five samples are listed in Table 2. Samples are chosen from both indoor and outdoor with each varying in characteristics. For each sample, we manually measure the slant angle ($\bar{\theta}$) using the tiltmeter, and as the baseline, we analyze the error from the computed slant angle. For M sample measurements, the error is computed as

4.2 | Qualitative wall extraction evaluation

We evaluate the wall extraction performance by comparing the original point cloud map (Figure 6A) and the extracted wall maps (Figure 6C). The first phase of the slant angle map generation is extracting walls from the initial point cloud map. We quantitatively examined extracted walls using the proposed two-phase automatic clustering.

The step-by-step wall extraction results are illustrated in Figure 6. Each map presents a zoomed view in the orange box. Most nonwall points, such as parked cars and small objects, have been removed from the

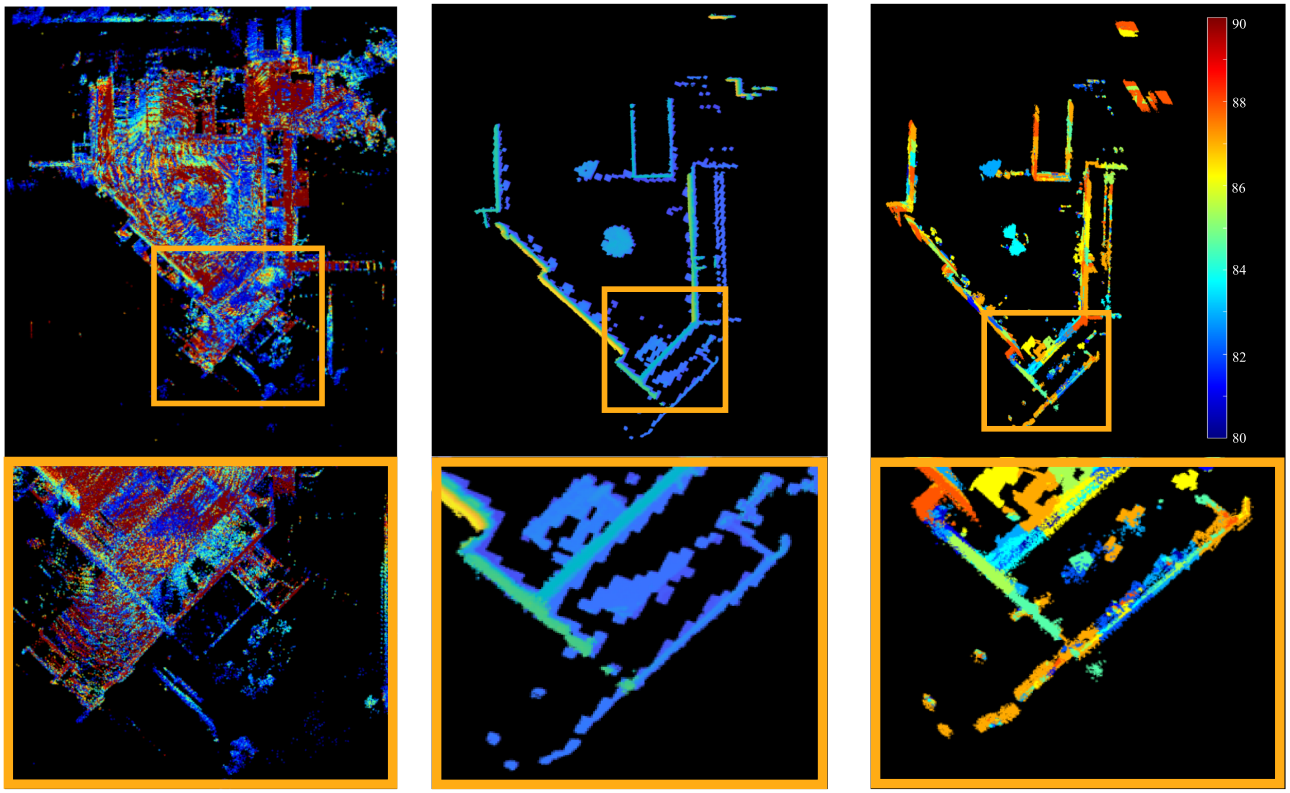

(A) Original SLAM map (B) Wall extraction map (C) Slant angle map

FIGURE 6 Comparison among original map, extracted wall map, and slant angel maps. The orange box indicates a zoomed view of each map

map after the wall extraction process. However, the tree in the center of the map has many points, so our method unfiltered them. As shown in Figure 6C, the map points are color coded using the estimated slant angle. The SLAM-induced slant angles vary from 80° to 90°. We will examine these slant angles quantitatively in the following section.

4.3 | Quantitative slant angle analysis

We conduct an experiment by dividing the sequence for a specific wall in the map to verify the accuracy of the slant angle estimation by measuring it directly using a tiltmeter (Figure 5). The tiltmeter used in the test is the Sincon DWL-200 with an error of about 0.1; thus, it is accurate enough as a baseline.

Table 3 presents the slant angle results from the five sample walls. The average value of the slant angle was derived using 10 tiltmeter measurements. Besides, the mean value was used after 10 trials and covered potential variance arising from the RANSAC. The largest error in the slant angle is 1.63° observed in the sample wall A and is attributed to the wall's curvature; however, it resides in a reasonable boundary (< 2°).

TABLE 3 Quantitative analysis on the estimated slant angle

Plane	Tiltmeter (°)	Proposed (°)	Error (°)
A	88.0	89.63	1.63
B	88.0	87.87	0.13
C	88.8	87.90	0.90
D	89.7	88.97	0.73
E	90.0	88.75	1.25

4.4 | Semantic nonwall objects elimination

Figure 7 shows the effect of the semantic classification (that is, wall vs. nonwall objects). The eigenvalue ratio classifier successfully segregated vegetation from wall objects, allowing the examination of the wall slant angle unaffected by bushes and trees. The nonwall objects and walls are denoted with red and blue dots, respectively.

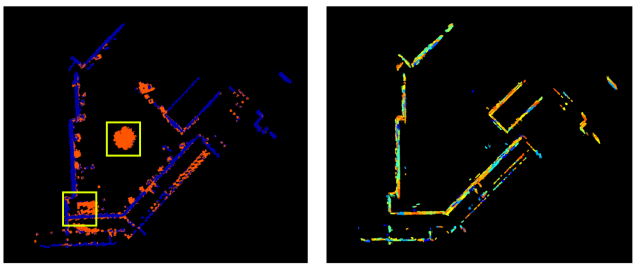

(A) Classification using singular value (B) Slant angle map after using singular value

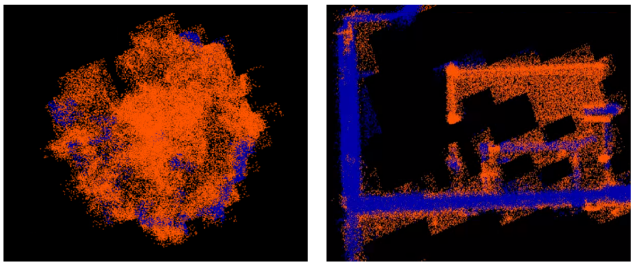

(C) Tree (D) Zoom view

FIGURE 7 (A) Separation of walls and nonwall objects using singular value. Red color means nonwall objects, and blue means walls. (B) The map after separation. (C,D) The zoomed view of the map showing tree, walls, and other objects in detail

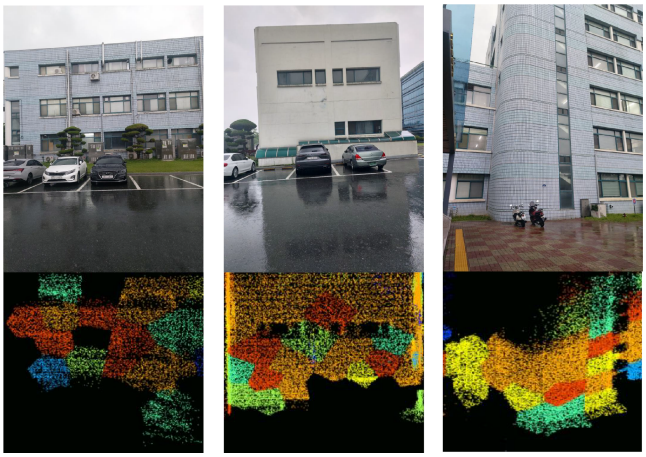

(A) Windows (B) Curve windows (C) Curve wall

FIGURE 8 The slant angle of irregular walls from front view. (A,B) windows and curved glass and (C) contain curved surfaces

Two zoomed views show a more detailed view after segmentation.

Figure 8 also shows that it detects uneven walls. Because the slant angle is calculated by dividing the wall by $\mathcal{P}_K$ points (Section 3.5), it demonstrates that the walls are robustly uneven, such as walls with windows and curved surfaces.

5 | CONCLUSION

This study presented a backpack-style mapping system equipped with LiDAR and IMU for measuring and estimating the slant angle. First, the wall points were initialized using two-phase clustering without knowing the cluster information in advance. Then, the RANSAC-based inlier sorting was applied before classifying the points by their associated covariance eigenvalues. During this step, vegetation was successfully removed, leaving only the clear wall points to be optimized for the normal vector. Combining the LiDAR-inertial SLAM framework produced a gravity-compensated 3D point cloud map for directly computing the slant angle of the large-scale environment with multiple walls. The extracted walls and their associated slant angles are estimated and evaluated using the tiltmeter. This system guarantees a large-scale and automatic slant angle estimation is possible.

ACKNOWLEDGMENT

This research was supported by the grant (21TSRD-B151228-03) from Urban Declining Area Regenerative Capacity-Enhancing Technology Research Program funded by Ministry of Land, Infrastructure, and Transport of Korean government.

AUTHOR CONTRIBUTIONS

Jeongyun Kim designed the analysis, contributed to data/analysis tools, and wrote the paper. Seungsang Yun collected the data and contributed to the experiment. Minwoo Jung collected the data and contributed to the experiment. Ayoung Kim conceived and preformed the analysis. Younggun Cho designed the analysis, collected the data, and wrote the paper.

ORCID

Younggun Cho https://orcid.org/0000-0003-2025-7770

REFERENCES

1. S. A. K. Tareen and H. M. Khan, *Novel slope detection and calculation techniques for mobile robots*, in Proc. Int. Conf. Robot. Artif. Intell. (Rawalpindi, Pakistan), Nov. 2016, pp. 158–163.
2. J. Lv et al., *Indoor slope and edge detection by using two-dimensional EKF-SLAM with orthogonal assumption regular paper*, Int. J. Adv. Robot. Syst. **12** (2015), no. 4, 44.
3. X. Meng et al., *A slope detection method based on 3D LiDAR suitable for quadruped robots*, in Proc. World Congr. Intell. Control Autom. (Gui-lin, China), June 2016, pp. 1398–1402.
4. Z. Mao et al., *Towards automated post-disaster damage assessment of critical infrastructure with small unmanned aircraft*

systems, in Proc. IEEE Int. Symp. Technol. Homeland Secur. (Madrid, Spain), Oct. 2018, pp. 1–6.
5. P. J. Besl and N. D. McKay, *A method for registration of 3-D shapes*, IEEE Trans. Pattern Anal. Mach. Intell. **14** (1992), no. 2, 239–256.
6. A. Segal, D. Hähnel, and S. Thrun, *Generalized-ICP*, in Proc. Robot.: Sci. Syst. V (Seattle, WA, USA), June 2009.
7. J. Zhang and S. Singh, *LOAM: Lidar odometry and mapping in real-time*, in Proc. Robot.: Sci. Syst. V (Berkeley, CA, USA), July 2014, 2014.
8. T. Shan and B. Englot, *LeGO-LOAM: Lightweight and ground-optimized lidar odometry and mapping on variable terrain*, in Proc. IEEE/RSJ Int. Conf. Intell. Robot. Syst. (Madrid, Spain), Oct. 2018, pp. 4758–4765.
9. T. Shan et al., *LIO-SAM: Tightly-coupled lidar inertial odometry via smoothing and mapping*, in Proc. IEEE/RSJ Int. Conf. Intell. Robot. Syst. (Las Vegas, NV, USA), Oct. 2021, pp. 5135–5142.
10. C. Forster et al., *On-manifold preintegration for real-time visual–inertial odometry*, IEEE Trans. Robot. **33** (2017), no. 1, 1–21.
11. C. Qin et al., *LINS: A lidar-inertial state estimator for robust and efficient navigation*, in Proc. IEEE Int. Conf. Robot. Autom. (Paris, France), May 2020, pp. 8899–8905
12. M. A. Fischler and R. C. Bolles, *Random sample consensus: A paradigm for model fitting with applications to image analysis and automated cartography*, Commun. ACM **24** (1981), no. 6, 381–395.
13. M. Ester et al., *A density-based algorithm for discovering clusters in large spatial databases with noise*, in Proc. Int. Conf. Knowl. Discov. Data Min. (California, USA), Aug. 1996, pp. 226–231.
14. J.-F. Lalonde et al., *Natural terrain classification using three-dimensional ladar data for ground robot mobility*, J. Field Robot. **23** (2006), no. 10, 839–861.

AUTHOR BIOGRAPHIES

Jeongyun Kim received the B.S. degree in the Department of Mathematical Sciences with dual degree in Electrical Engineering, KAIST, Daejeon, Korea, in 2020. Currently, he is an M.S. student in the Department of Civil & Environmental Engineering, KAIST. His research interests include simultaneous localization and mapping.

Seungsang Yun received the B.S. degrees in the Department of Mechatronics Engineering from Chungnam National University, Daejeon, Korea, in 2020. Currently, he is an M.S. student in the robotics program, KAIST. His research interests include simultaneous localization and mapping using thermal infrared cameras and autonomous robots.

Minwoo Jung received the B.S. degree in Department of Civil and Environmental Engineering from KAIST, Daejeon, Korea, in 2021. Currently, he is an M.S. student in the Department of Civil and Environmental Engineering, KAIST. His research interests include simultaneous localization and mapping using LiDAR and high definition maps.

Ayoung Kim received B.S. and M.S. degrees in Mechanical Engineering from Seoul National University, Seoul, Korea, in 2005 and 2007, respectively, and the M.S. degree in Electrical Engineering and the Ph.D. degree in Mechanical Engineering from the University of Michigan (UM), Ann Arbor, in 2011 and 2012, respectively. Currently, she is an associate professor in the Department of Civil and Environmental Engineering with a joint affiliation at KI robotics, Korea Advanced Institute of Science and Technology (KAIST). Her research interests include visual simultaneous localization and mapping and navigation.

Younggun Cho received the B.S. degree in Electrical Engineering from Inha University, Incheon, Korea, in 2013, and the M.S. degree in Electrical Engineering in 2015 and a Ph.D. degree in Civil and Environmental Engineering with a dual degree in robotics program (2020) from the Korea Advanced Institute of Science and Technology (KAIST), Daejeon, Korea. He is currently an assistant professor with the Department of Robotics Engineering at Yeungnam University, Gyeongsan, South Korea. His current research interests include robust sensing, long-term autonomy, and visual simultaneous localization and mapping.